

Mira Ceti, atypical archetype

P.T. Nhung [★], D.T. Hoai [†], P. Tuan-Anh, P. Darriulat, P.N. Diep, N.B. Ngoc, and T.T. Thai

*Department of Astrophysics, Vietnam National Space Center, Vietnam Academy of Science and Technology,
18, Hoang Quoc Viet, Nghia Do, Cau Giay, Ha Noi, Vietnam*

Accepted XXX. Received YYY; in original form ZZZ

ABSTRACT

With the aim of unravelling the complexity of the morpho-kinematics of the circumstellar envelope (CSE) of Mira Ceti, we review, extend and possibly revisit ALMA millimetre observations of the emission of the SiO(5-4) and CO(3-2) molecular lines, including a new analysis of the optically thin $^{13}\text{CO}(3-2)$ emission. In agreement with observations at shorter wavelengths, we give evidence for confinement of a dense gas volume within ~ 50 au from the star and for a broad SiO line-width within ~ 15 au. We show that the mass loss rate is episodic and takes the form of clumps having a very low SiO/CO abundance ratio. We evaluate the current mass loss rate as $(8 \pm 4) \times 10^{-8} M_{\odot} \text{ yr}^{-1}$, much smaller than usually assumed. We argue that the SiO emission observed in the south-western quadrant is not related to the mechanism of generation of the nascent wind but results from dust grains outgassing SiO molecules, in support of an earlier interpretation in terms of a mass ejection that occurred eleven years before the observations. We remark that Mira Ceti is not a good archetype in terms of its wind: lower mass AGB stars, with a mass loss rate at the level of a few $10^{-7} M_{\odot} \text{ yr}^{-1}$ and preferably no companion are better suited for developing models of the very complex gas-dust chemistry at stake in the CSE of oxygen-rich AGB stars.

Key words: stars: AGB and post-AGB – circumstellar matter – stars: individual: Mira Ceti – radio lines: stars

1 INTRODUCTION

The present article aims at reviewing and improving our knowledge of the mechanisms governing the generation of the nascent wind of Mira Ceti (Mira A), one of the most observed AGB stars, remarkable for the large amplitude of its variability (~ 8 mag), and known to be accompanied by a distant companion (Mira B, ~ 70 to 80 au away). Basic parameters are listed in Table 1. In the present article we adopt a distance of 100 pc, 10 mas spanning 1 au. While Vanture et al. (1991) have detected technetium in the Mira A spectrum, conflicting negative results have been obtained by Kipper (1992); moreover Hoai et al. (2020), hereafter referred to as “paper I”, measured a $^{12}\text{CO}/^{13}\text{CO}$ abundance ratio of 12 ± 2 , a rather low value for a star supposed to have already experienced the third dredge up. The time spent by Mira A on the AGB is therefore uncertain; it is at least $30\,000$ years, as testified by the turbulent wake detected by Galex (Martin et al. 2007), which traces its interaction with the ISM; but this is not much in comparison with the time it takes to reach the third dredge up. Moreover, the mass loss rate is also very uncertain, the estimates commonly quoted (Table 1) being indirect and assuming, in particular, a spherically symmetric wind.

Table 1. Some basic parameters.

| Quantity | Value | Reference |
|------------------|-------------------------------------|-----------------------------|
| Distance | 92 ± 10 pc | van Leeuwen (2007) |
| | 110 ± 9 pc | Haniff et al. (1995) |
| Spectral type | M5-9IIIe+DA | Skiff (2014) |
| Pulsation period | 333 d | Templeton & Karovska (2009) |
| Temperature | 2900 to 3200 K | Woodruff et al. (2004) |
| Mass-loss rate | A few | Ryde & Schöier (2001) |
| | $10^{-7} M_{\odot} \text{ yr}^{-1}$ | Heras & Hony (2005) |

1.1 Binarity related features and past history

In the present article, we focus on an exploration of the mechanism currently governing the formation of the nascent wind of Mira A. As its companion, Mira B, is far away, it is known to have little impact: binarity related features are expected to be largely irrelevant. Yet, they represent such an important fraction of the published literature that we summarize briefly the main results in the present section and list in Table 2 the corresponding references.

The first image showing a clear separation between Mira A and its companion was obtained in 1997 with the HST and the pair has been resolved later at many other wavelengths. A clear bridge linking the two stars has been observed in X-ray by Chandra, in UV by the HST and in the infrared by the VLT. Mira B is generally considered to be a White Dwarf surrounded by a thin accretion disc rotating at high velocity and its highly variable UV emission has

[★] E-mail: ptt Nhung@vnsc.org.vn

[†] E-mail: dthoai@vnsc.org.vn

been claimed to dominate over that of Mira A. Both statements have been disputed, however: Ireland et al. (2007) have argued that Mira B is a Main Sequence star and Montez et al. (2017) have questioned the supposed dominance of the UV emission of Mira B over Mira A. As Mira is moving at very high velocity through the interstellar medium it leaves a turbulent wake behind it that has been detected in the UV with evidence for a bow shock; the astropause has been detected in the FIR. Closer to the star, observations in the FUV and H α have revealed the possible presence of a fast bipolar outflow. The Mira pair is thought to display occasional nova-like eruptions and a soft X ray outburst, probably associated with mass ejection, was observed in 2003.

At millimetre wavelengths, the companion is detected separately from the AGB star, with a clear bridge linking the two stars, and its presence is seen to influence the morpho-kinematics of the wind, in particular by focusing the wind of Mira A (Nhung et al. 2016). Yet, the impact of binarity on the morpho-kinematics of the CSE has been shown to be small (paper I, Vlemmings et al. 2015; Nhung et al. 2016): it is limited to Mira B focusing the wind of Mira A that blows toward it, part of which being accreted, but is unrelated to the overall morpho-kinematics of the CSE. In particular a southern arc, which was described by Ramstedt et al. (2014) as the birth of a spiral, has been shown to have no simple relation with Mira B and to wind in the wrong direction to be interpreted as a Wind Roche Lobe Overflow spiral.

The orbit has a semi-major axis of 70 to 80 au with a period at 500 yr scale and is inclined by some 60° with respect to the plane of the sky. From the observation of the blue-shifted wind blowing from Mira A to Mira B (paper I, Nhung et al. 2016), we know that Mira B is closer to us than Mira A by some 60 au. The mass of Mira A is ~ 2 solar masses, that of Mira B ~ 0.7 solar masses; the escape velocity at 25 au from a 2 solar masses star is ~ 12 km s $^{-1}$.

1.2 Shocks and dust formation in the close neighbourhood of Mira A

We review below what is known of the physics and chemistry at stake within a few au from the surface of Mira A. In contrast with the preceding section, it is of direct relevance to our study. Table 3 lists the main results and associated references.

From infrared to millimetre wavelengths, the latter probing the proximity of the stellar surface with vibrationally excited molecular lines or continuum emission, all studies show the importance of pulsation- and shock-induced dynamics in levitating the molecular atmosphere. They reveal a complex dynamics and grain chemistry, influenced by variability, displaying significant inhomogeneity and suggesting the presence of shocks related to star pulsations. Evidence is found for short time variability (at month scale), occasional gas in-fall, hot spots covering a small fraction of the stellar disc, radial velocities at the 10 km s $^{-1}$ scale, all revealing the impact of shocks associated with pulsations and convective cell ejections. A consequence on the millimetre observation of the emission of molecular lines is the presence of large Doppler velocity wings near the line of sight crossing the stellar disc in its centre (paper I).

Another feature revealed by most studies is an abrupt decline of the gas emission of SiO and other molecules at distances from the star in excess of some 5 to 6 au. Dust is observed to cluster near the edge of this region. No convincing interpretation has been proposed, whether in terms of shock wave, of recent increase of mass loss or of dust condensation. The gas phase of Al-bearing molecules is seen to deplete very close to the star, within 3 to 4 au, revealing their condensation in dust grains, in contrast with Ti-bearing molecules,

which are thought to play essentially no role in the formation of dust. Evidence for the presence of large dust grains, at 0.1 micron scale, within a very few au from the radiosphere, is obtained from the study of continuum emission as well as from the observation of polarized light. Observation of SiO masers suggests the presence of rotation at some 7 au from the centre of the star. Finally, we note that there have been speculations about a possible magnetic origin of hot spots and/or rotation in Mira A (Thirumalai & Heyl 2013).

1.3 Morpho-kinematics of the CSE beyond 20 au from Mira A

ALMA observations of the CO(3-2) and SiO(5-4) line emissions have been analysed in paper I and by Ramstedt et al. (2014) and Nhung et al. (2016). A very complex morpho-kinematics is observed, witness of several past episodes of enhanced mass loss; however, by limiting the range of Doppler velocities to $|V_z| < 4$ km s $^{-1}$, one can reasonably well select the more recent emission. In particular it excludes the contribution of a blue-shifted bubble, or ring, emitted some 2'000 years ago, together with red-shifted fragments probably ejected at the same epoch. At shorter distances from Mira A, within some 250 au, two broad outflows are seen in the south-western and north-eastern quadrants. They display important inhomogeneity, the north-eastern outflow being strongly depleted at distances between ~ 100 au and ~ 200 au. The emission of the SiO(5-4) line is confined to the south-western outflow for distances from the star in excess of some 50 au. Several interpretations have been suggested to explain these observed features, none of which, however, can be considered as well established. In paper I, we remarked that the CO(3-2) emission seems to be enhanced in the orbital plane of the AB pair; however, the long orbital period, at 500 yr scale, makes it difficult to conceive a sensible scenario. We also suggested a mechanism for the SiO and CO emissions in the south-western quadrant that relates to the 2003 mass ejection associated with the detection of a soft X ray outburst, but again lacking a solid basis.

1.4 Outline of the article

The aim of the article is to contribute to unravelling the complexity of the observed morpho-kinematics of the CSE of Mira Ceti. For convenience for the reader, the present introduction has given a review of recent publications of relevance. Section 2 revisits an analysis of the SiO line width within 15 au from the star, strengthening earlier results and suggesting the presence of rotation. Section 3 presents a detailed analysis of the emission of the $^{13}\text{CO}(3-2)$ line, on which many of the results presented in the article, in particular an evaluation of the mass loss rate, are based. Section 4 addresses the peculiarities of the observed SiO emission after having shown that they are real and not artefacts of the imaging process: the confinement of high gas density within some 50 au from the star, the particularly low SiO/CO abundance ratio and the complex, unexpected and different patterns displayed by CO and SiO emission in the south-western quadrant. Section 5 summarizes the results and concludes.

2 SIO(5-4) LINE WIDTH IN THE 5 TO 15 AU RANGE

As we have seen in the preceding section, one of the best established and non-controversial features of the dynamics of the inner layer of the CSE is the presence of important shocks induced by pulsations

Table 2. Binarity related features. Events of a general episodic nature are also included.

| Reference | Instrument | Observation | Scale | Main results |
|-----------------------------|-----------------------------|--|----------------|---|
| Reimers & Cassatella (1985) | IUE | UV continuum | - | Suggests accretion disc around Mira B |
| Karovska et al. (1997) | HST/FOC | Visible & UV | 30-45 mas | First resolved image of the pair |
| Wood et al. (2002) | HST/STIS | Ly α fluoresced H $_2$ lines | - | Evidence for strong variability of Mira B accretion luminosity. Speculate on Mira B wind |
| Prieur et al. (2002) | PISCO | Visible speckle | - | First orbit |
| Karovska et al. (2005) | Chandra ACIS/S | Soft X-ray | - | Soft X-ray outburst in Mira A, suggests large mass ejection |
| Matthews & Karovska (2006) | VLA | Continuum 1 cm | 250 mas | First separation of the pair at cm wavelength |
| Wood & Karovska (2006) | HST FUSE | UV FUV | - | Evidence for variability of Mira B UV emission |
| Ireland et al. (2007) | Keck Gemini South/T-reCS | 10-13 μ m 8-18 μ m | \sim 200 mas | Claim that Mira B is a \sim 0.7 M_{\odot} main sequence star surrounded by a \sim 10 au radius disk |
| Martin et al. (2007) | Gallex | FUV | 2 $^{\circ}$ | Bow shock and turbulent wake from interaction Mira/ISM |
| Ueta (2008) | Spitzer/MIPS | FIR 160 μ m | 10 arcmin | Observation of the astropause |
| Meaburn et al. (2009) | MES-SPM S. Pedro Martir | H α | - | \sim 1000 years old bipolar outflow tilted at $69^{\circ} \pm 2^{\circ}$ to the sky plane with velocity of 160 ± 10 km s $^{-1}$ |
| Sokoloski & Bildsten (2010) | Nickel telescope | Optical | - | Evidence for rapid optical variability. Claim that Mira B is a WD. |
| Mayer et al. (2011) | Herschel PACS | 70 & 160 μ m | 2 arcmin | Evidence for arcs, in particular a pair of back-to-back arcs, south-west/north-east, \sim 1 arcmin away from the star |
| Vlemmings et al. (2015) | ALMA | Continuum 3.2 & 1.3 mm | 0.3-0.7 arcsec | End October 2014 separation=472 mas at PA=98.6 $^{\circ}$ |
| Planesas et al. (2016) | ALMA | Continuum 0.89 & 0.44 mm | 0.2-0.3 arcsec | AB masses are \sim 2 and 0.7 M_{\odot} . Orbit needs corrections |

and convection cell ejections. It is a common feature of all O-rich AGB stars that have been observed with high angular and spectral resolutions. At millimetre wavelengths, its impact on the line profile of single dish observations, in the form of broad Doppler velocity wings, had been noticed early and properly interpreted as suggesting that the emission occurs close to the star where SiO grains have not yet fully formed and is somehow related to star pulsations (Winters et al. 2003). De Vicente et al. (2016) observed their presence in the SiO(1-0) emission of five oxygen-rich AGB stars, Mira A, R Hya, R Leo, W Hya and RS Cnc, and quoted total fluxes (normalised to a distance of 100 pc) of 4.6, 7.0, 10.6, 18.3, and 6.3 Jy km s $^{-1}$, respectively. However, when the presence of high Doppler velocity wings close to the line of sight crossing the star in its centre was first noticed on R Dor (Decin et al. 2018), it was not immediately understood.

On Mira A, their presence was first revealed (paper I) in the emission of the SiO(5-4) molecular line. In the present section we revisit and refine this analysis. We refer the reader to paper I for details of the observations and data reduction. We recall that the beam is 6×3 au 2 FWHM and that Doppler velocities are measured with respect to a systemic velocity of 47.7 km s $^{-1}$ with respect to the local standard of rest. We use coordinates with x pointing east, y pointing north and z pointing away from us.

Figure 1 displays, in each of four quadrants, Doppler velocity spectra averaged in 3 au wide annular rings centred on Mira A with mean radii increasing from 2.5 au (blue) to 21.5 au (red) in steps of 1 au. A cut at 3σ is applied to the data. The dependence on R (projected distance from the centre of Mira A) of the full-width at 1/5 maximum of the spectra, displayed in Figure 2 left, shows that the line width decreases from maximum to minimum when R spans from \sim 5 au to \sim 15 au. In principle, part of the line width might be due to a velocity gradient within a ring, such as produced by rotation. In order to assess the importance of such a contribution,

we repeat the analysis by re-centring, in each 3×3 au 2 pixel, the observed Doppler velocity spectrum on its mean value. The effect is minimal, as illustrated in Figure 2 middle-left with the example of the ring 6 au $< R < 12$ au. The decrease of the rms deviation with respect to the mean never exceeds 0.1 km s $^{-1}$ and, on average, is only 0.05 km s $^{-1}$.

This result strengthens the conclusion that, with a resolution of \sim 3 au, the line width becomes very broad at projected distances smaller than \sim 15 au, reaching over 20 km s $^{-1}$ at $R < \sim$ 5 au. At the same time, it makes it difficult to detect a small velocity gradient, in particular the possible presence of rotation; such rotation would cause the mean Doppler velocity, $\langle V_z \rangle$, to have a sine wave dependence on position angle ω (measured counter-clockwise from north) at distances from the star where rotation is significant. We illustrate it using a ring covering 3 au $< R < 10$ au: Figure 2 middle-right shows that the spectrum in such a ring is very broad, at the scale of 20 km s $^{-1}$. Moreover, it is rather flat in comparison with the spectrum in the broader circle $R < 20$ au: if one evaluates $\langle V_z \rangle$ over too short an interval of V_z , one is not sensitive to a possible shift; one needs therefore to calculate it over a broad interval, implying a large uncertainty on the result. This is illustrated in Figure 3, which displays maps of $\langle V_z \rangle$ calculated over different intervals of V_z . For intervals broader than $\sim \pm 10$ km s $^{-1}$, the map displays a pattern typical of rotation about an axis projecting in the north-east/south-west direction; but for intervals narrower than $\sim \pm 7$ km s $^{-1}$, the evidence is much weaker. Figure 2 right shows the dependence on ω of $\langle V_z \rangle$ evaluated in intervals of ± 17 km s $^{-1}$ and ± 10 km s $^{-1}$, respectively. The best sine wave fits are $\langle V_z \rangle = -0.53 + 0.54 \sin(\omega - 40^{\circ})$ and $-0.47 + 0.89 \sin(\omega - 41^{\circ})$ km s $^{-1}$, respectively. Uncertainties accounting for the systematic effects of choosing different intervals of R and/or V_z are estimated as $\sim \pm 0.2$ km s $^{-1}$ on the projected velocity and $\sim \pm 15^{\circ}$ on the position angle of the projected rotation axis. The offsets may reveal an overestimate of the systemic veloc-

Table 3. Inner CSE of Mira A (within a few au).

| Reference | Instrument | Observation | PSF (mas ²) | Main results |
|---|----------------------|---|--|--|
| Cotton et al. (2004) Cotton et al. (2006) | VLBA | SiO maser | 1 | Possible rotation |
| Chandler et al. (2007) | ISI | Continuum 11.15 μm | <100 | Suggest periodic emission of dust with a frequency of ~ 10 yr |
| Matthews et al. (2015) | JVLA ALMA | Continuum 6.7, 3.1 & 1.3 mm | 45 \times 34 79 \times 58 32 \times 23 | Radio photosphere is slightly elongated, by ~ 10 -20%. Evidence for brightness non-uniformities on the surface of Mira. |
| Vlemmings et al. (2015) | ALMA | Continuum 3.2 & 1.3 mm | 79 \times 58 32 \times 23 | Possible evidence for shock heating. Hotspot likely due to magnetic activity possibly related to the 2003 X-ray flare. |
| Kamiński et al. (2016) | ALMA | AlO($N=6-5$) | 34 \times 24 | Consistent with gas phase AlO starting to deplete into dust at ~ 25 mas. Strong variability and inhomogeneity likely to reveal shocks in the stellar photosphere. |
| Wong et al. (2016) | ALMA | SiO, H ₂ O | 34 \times 24 | Absorption over stellar disc shows optically saturated SiO (²⁸ SiO and ²⁹ SiO(5-4) are \sim identical). No sign of a non zero terminal velocity in absorption spectra. Evidence for in-fall. SiO($v=0,2$) and H ₂ O($v_2=1$) spectra well described by simple radiative transfer. SiO abundance drops by some 2 orders of magnitude beyond ~ 60 mas. Presence of a shock. |
| Planesas et al. (2016) | ALMA | Continuum 0.89 & 0.44 mm | 310 ² & 180 ² | Continuum emission consistent with models of radio photosphere with spectral index close to 2 |
| Wittkowski et al. (2016) | 3D model | | | Observational support for shocks induced by convection and pulsation to be spherically. Unlike for red supergiants, the pulsation- and shock-induced dynamics can levitate the molecular atmosphere to extensions that are consistent with observations |
| Khouri et al. (2016) | ALMA | CO($v=1,3-2$) | 540 ² | Evidence for variability |
| Kamiński et al. (2017) | ALMA | TiO, TiO ₂ | 158 \times 127 | Gas phase Ti-bearing molecules consistent with models with shocks. High abundance suggests that Ti oxides play negligible role in dust formation |
| Khouri et al. (2018), Khouri et al. (2019) | VLT/SPHERE ZIMPOL | 0.65, 0.75 & 0.82 μm | 30 ² | Evidence for high gas density up to steep decline at ~ 60 mas with dust grains clustering at the edge of this region. Suggest propagation of a shock front or a recent increase of mass loss rate. Al ₂ O ₃ grains within 84 mas must have an average size $< 0.02 \mu\text{m}$; grains with sizes $\sim 0.1 \mu\text{m}$ would account for less than 1% of the aluminium atoms. |
| | ALMA | ¹³ CO(3-2) AlO($N=9-8$) SO($N_f=8_8 - 7_7$) CO($v=1,3-2$) | 33 \times 19 | |
| Vlemmings et al. (2019) | ALMA | Continuum 0.9, 1.4 & 2.3 mm | 33 \times 23 65 \times 35 69 \times 57 | Contrary to Matthews et al. (2015), disc is circular with little inhomogeneity but data need a layer of increased continuum opacity probably related to convective shocks. |
| Perrin et al. (2020) | IOTA | 1.65 μm | 10 \times 23 | Consistent with clumpiness of dust production and combination of pulsation and convection. |

ity: we use the value obtained by Khouri et al. (2018) from a fit to the CO($v=1,3-2$) line emission in the close environment of the star. This is 1.0 km s^{-1} larger than obtained by Wong et al. (2016) from a fit to the SiO(5-4) line over a large field of view: the uncertainty on this number may be as large as $\pm 1 \text{ km s}^{-1}$.

The sine wave fits suggest the presence of rotation within some 15 au from the centre of the star with a projected velocity of $0.7 \pm 0.2 \text{ km s}^{-1}$ about an axis projecting $40^\circ \pm 15^\circ$ east of north. It is in agreement with the values quoted by Cotton et al. (2004, 2006): $1.5 \pm 0.9 \text{ km s}^{-1}$ and $17 \pm 36^\circ$, respectively. Rotation is commonly interpreted as evidence for the presence of a companion; in the present case, however, such a possible rotation, if confirmed, could not have anything to do with Mira B, which is much farther away and rotates in opposite direction.

In summary, this re-analysis of the emission of the SiO(5-4) line has strengthened the evidence for intrinsically broad line widths within ~ 15 au from the line of sight crossing Mira A in its centre. At the same time, it has revealed the possible existence of rotation in this same central region, about an axis projecting $40^\circ \pm 15^\circ$ east of north with a projected velocity of $0.7 \pm 0.2 \text{ km s}^{-1}$, in agreement with results obtained from the observation of SiO masers. However, the

difficulty of this measurement has been underlined and the evidence for the presence of rotation needs to be confirmed by independent observations before being accepted.

3 ¹³CO(3-2) EMISSION

As mentioned in Section 1.3, the emission of the ¹²CO(3-2) line has been studied by Ramstedt et al. (2014), Nhung et al. (2016) and in paper I; in the latter, we have also reduced observations of the ¹³CO(3-2) emission, made within the same ALMA project, and have evaluated the ¹²CO/¹³CO ratio as 12 ± 2 . In the present section, we refine this analysis with the aim of obtaining new information of relevance to the generation of the nascent wind. Imaging was done using GILDAS with natural weighting, giving a nearly circular beam with a diameter of ~ 0.38 arcsec FWHM. The brightness distribution is displayed in Figure 4 left, giving evidence for a noise σ of 5 mJy beam^{-1} . Table 4 lists some parameters of relevance to the comparison between ¹²CO(3-2) and ¹³CO(3-2) emissions. Their values are similar, with the result that the ratio between the two emissions is nearly independent from temperature and, in the optically thin limit, provides a direct measure of the isotopic ratio.

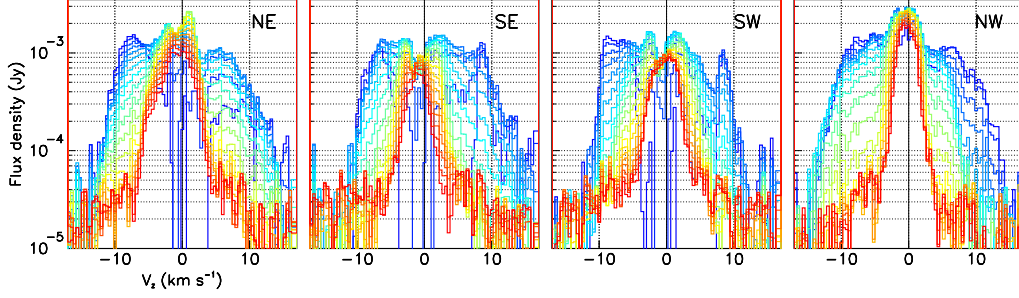


Figure 1. SiO(5-4) emission of Mira A. Doppler velocity spectra averaged in quadrants of 3 au wide annular rings centred on Mira A with mean radii increasing from 2.5 au (blue) to 21.5 au (red) in steps of 1 au. (Reproduced from Figure A2 of paper I)

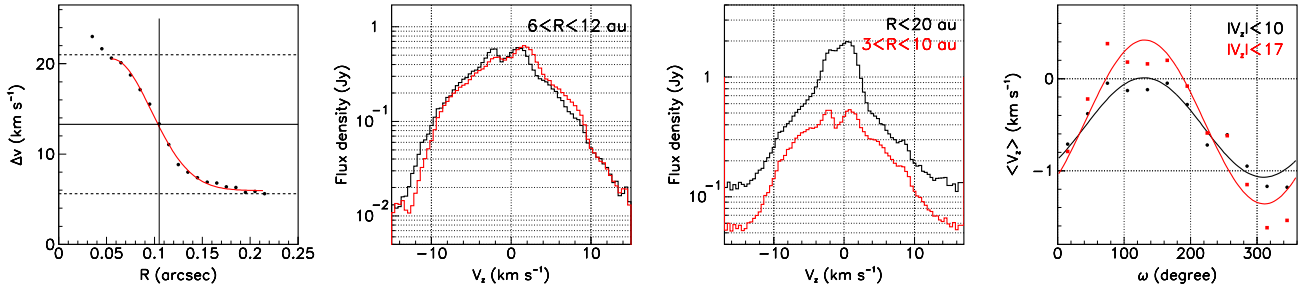


Figure 2. SiO(5-4) emission of Mira A. Left: Dependence on R of the full-width at 1/5 maximum of the spectra displayed in Figure 1 (all four quadrants together, reproduced from Figure 14d of paper I). Middle-left: Doppler velocity spectrum observed in the ring $6 \text{ au} < R < 12 \text{ au}$ before (black) and after (red) re-centring. Middle-right: Doppler velocity spectra evaluated in the circle $R < 20 \text{ au}$ and in the ring $3 \text{ au} < R < 10 \text{ au}$. Right: dependence of the mean Doppler velocity on position angle ω in the ring $3 \text{ au} < R < 10 \text{ au}$. The lines are sine wave best fits.

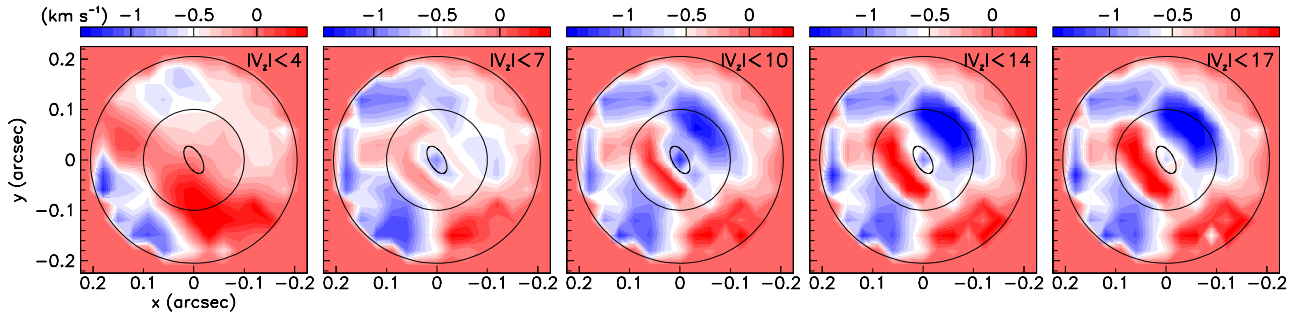


Figure 3. Maps of $\langle V_z \rangle$ evaluated over different intervals of V_z as indicated on top of each panel. The circles in the centre of each panel have a radius of 10 au. The ellipse in the centre of each panel shows the beam size.

3.1 Comparing $^{13}\text{CO}(3-2)$ and $^{12}\text{CO}(3-2)$ emissions

As the $^{13}\text{CO}(3-2)$ emission is typically one order of magnitude smaller than the $^{12}\text{CO}(3-2)$ emission, we limit the present study (in addition to the restriction to the Doppler velocity interval of $\pm 4 \text{ km s}^{-1}$) to the central region where the intensity of the $^{12}\text{CO}(3-2)$ emission exceeds $10 \text{ Jy arcsec}^{-2} \text{ km s}^{-1}$. Its map is displayed in the left panel of Figure 5. It is elongated in the north-east/south-west direction and covers fragments that were identified in paper I and were given names of south-western outflow (SWO), north-eastern outflow (NEO) and north-eastern arc (NEA) respectively. In what follows we refer to it as region C (for central), implying in addition that the inequality $|V_z| < 4 \text{ km s}^{-1}$ is satisfied. Note that the reduction of both ^{12}CO and ^{13}CO observations was made without continuum

subtraction. In the $|V_z| < 4 \text{ km s}^{-1}$ interval, the contribution of the continuum to region C is $\sim 2.7 \text{ Jy km s}^{-1}$.

The radial distributions of the emissions in region C of the $^{12}\text{CO}(3-2)$ and $^{13}\text{CO}(3-2)$ lines are compared in the central panel of Figure 4. They give evidence for an important concentration of CO molecules in the close neighbourhood of the star. Extrapolation to $R=0$ of the intensity observed in the ring $1 < R < 2 \text{ arcsec}$ gives excesses of 28.9 and 6.4 Jy km s^{-1} for $^{12}\text{CO}(3-2)$ and $^{13}\text{CO}(3-2)$ respectively; the $^{13}\text{CO}/^{12}\text{CO}$ ratio is large, ~ 0.22 , implying important absorption. Evidence for such confinement had been previously obtained by Khouiri et al. (2018) from high angular resolution ALMA observations of the $^{12}\text{CO}(\nu=1,3-2)$ and $^{13}\text{CO}(3-2)$ line emissions; the beam was $\sim 30 \times 20 \text{ mas}^2$ but the maximal recoverable scale was only $\sim 0.4 \text{ arcsec}$: the present analysis provides a useful complement to their work, extending the reach to over 3 arcsec. Doppler velocity

Table 4. Parameters of relevance to the comparison between the $^{13}\text{CO}(3-2)$ and $^{12}\text{CO}(3-2)$ emissions.

| Line | $^{12}\text{CO}(3-2)$ | $^{13}\text{CO}(3-2)$ |
|--------------------------------|--------------------------------------|--------------------------------------|
| Beam | $0.39 \times 0.36 \text{ arcsec}^2$ | $0.40 \times 0.37 \text{ arcsec}^2$ |
| Frequency | 345.8 GHz | 330.6 GHz |
| Noise (σ) | 14 mJy beam^{-1} | 5 mJy beam^{-1} |
| Einstein coefficient, A_{ji} | $2.50 \times 10^{-6} \text{ s}^{-1}$ | $2.18 \times 10^{-6} \text{ s}^{-1}$ |
| Upper level energy, E_u | 33.2 K | 31.7 K |

spectra are shown in the right panel of Figure 4; from earlier studies of the $^{12}\text{CO}(3-2)$ emission, the features seen on the blue-shifted and red-shifted wings are associated with fragments emitted some few 1'000 years ago and the cut $|V_z| < 4 \text{ km s}^{-1}$ is effective at selecting the central, more recent emission.

The maps of the intensity in region C of the $^{13}\text{CO}(3-2)$ emission and of its ratio to the $^{12}\text{CO}(3-2)$ emission are displayed in the central and right panels of Figure 5. The latter shows significant non-uniformity, as further illustrated in the left panel of Figure 6 displaying the correlation between the intensities of the two emissions in region C. Their ratio spans a broad range of values; the central panel of Figure 6 shows its correlation with the intensity of the ^{13}CO emission. In the optically thin approximation the intensity of the ^{13}CO emission is proportional to the column density and the absorption of the ^{12}CO emission is therefore expected to be larger for larger values of the intensity of the ^{13}CO emission. This is indeed what the central panel of Figure 6 shows, with the $^{13}\text{CO}/^{12}\text{CO}$ intensity ratio increasing with the ^{13}CO intensity. Yet, we note that the left panel of Figure 6 shows a distinctive feature of high $^{13}\text{CO}/^{12}\text{CO}$ ratio in a region associated with the part of the Mira A wind blowing toward Mira B but we failed to find something special about it: as an example of the many distributions that we examined in this context, we compare in the right panel of Figure 6 the x' distributions (see below) of the intensities of the ^{12}CO and ^{13}CO emissions in the region of the data cube corresponding to the wind blowing toward Mira B.

In order to understand in finer detail how the $^{13}\text{CO}/^{12}\text{CO}$ intensity ratios are distributed among the fragments that make region C, we take advantage of the approximate symmetry displayed by region C about an axis x' making an angle of $\sim 35^\circ$ north of east: we use coordinates (x', y') rotated clockwise by 35° from (x, y) to explore the morpho-kinematics. This is done in Figure 7, which uses x' (pointing north-east) as axis of abscissa and y' , normal to it and pointing north-west, as axis of ordinate. PV maps of the Doppler velocity V_z vs x' and y' respectively, restricted to region C, are displayed for the $^{12}\text{CO}(3-2)$ emission, for the $^{13}\text{CO}(3-2)$ emission and for their ratio. This representation makes it easier to identify the different fragments revealed in paper I: a north-eastern arc (NEA) and a pair of outflows, north-eastern (NEO) and south-western (SWO). It also shows clearly an outflow that blows in the south-eastern direction, along $y' < 0$, and is slightly blue-shifted: we refer to it as the south-eastern outflow (SEO). Most of it is the wind of Mira A focused by Mira B that has been studied in detail in paper I; we shall comment on it in Section 3.2 when discussing the mass loss rate. In addition, the representation using rotated coordinates suggests separating a blue-shifted stream from the south-western outflow; it was clearly visible as a blob in the V_z vs ω map but had been grouped together with the south-western outflow in paper I. We prefer to give it a proper identity and we refer to it as south-western stream (SWS).

Another advantage of this representation is to make it clear that the NEA and the SWO are nearly detached from the central

emission: they are associated with masses of gas that have been emitted several decades ago. In contrast, the NEO, SEO and SWS are in continuity with the central emission and are therefore associated with on-going mass loss. Together with the stream of wind focused by Mira B, they are blowing toward the blue hemisphere and are therefore expected to be prone to absorption. As a further illustration of this result, we display in Figure 8 projections on the x' and y' axes for three separate intervals of Doppler velocity: -4 to -1 km s^{-1} , -1 to 1 km s^{-1} and 1 to 4 km s^{-1} .

For each of the fragments making up region C, we evaluate the $^{12}\text{CO}(3-2)$ and $^{13}\text{CO}(3-2)$ emissions and calculate their ratio. The result is listed in Table 5, which defines which data cube elements are included in the definition of each fragment; in addition to be part of region C, their coordinates x' , y' and V_z must satisfy inequality relations listed in the table. The isotopic ratios vary between 0.10 and 0.15; they are larger for the SEO and the NEO, which are blue-shifted, than for the south-western outflow. Paper I quotes a typical value of $1/7 \sim 0.14$.

3.2 Mass loss rate

The observed fragmentation and variability of the Mira wind implies that some caution needs to be exerted when defining a mass loss rate. We first limit our ambition to evaluating it in the south-eastern quadrant, $y' < 0$; we see from Figure 7 that it is dominated by the SEO and confined to Doppler velocities between -3 and 1 km s^{-1} . We use the ^{13}CO data in order to be reasonably free from absorption: in the optically thin approximation, the total flux provides a direct measure of the number of molecules. Precisely, for a temperature of $\sim 100 \text{ K}$, an emission of 1 Jy km s^{-1} requires the presence of 2.0×10^{46} ^{13}CO molecules. Assuming a $^{12}\text{CO}/^{13}\text{CO}$ isotopic ratio of 12 and an abundance ratio $^{12}\text{CO}/\text{H}$ of 2×10^{-4} , this implies a total hydrogen mass of $2.0 \times 12 \times \frac{1}{2} \times 10^{50} = 1.2 \times 10^{51}$ proton masses, or 1.0×10^{-6} solar masses. We recall that about a century ago, Mira B was 70 to 80 au south of Mira A in the sky plane. Over the past century, it moved in the blue-shifted direction on an orbit inclined by $\sim 60^\circ$ with respect to the plane of the sky, and is presently nearly east of Mira A. The Doppler velocity of the wind is currently close to its space velocity and of the order of 3 km s^{-1} . It projects on the plane of the sky as $\sim 1.5 \text{ km s}^{-1}$ at the time of the observation and as $\sim 3 \text{ km s}^{-1}$ a century ago. On average over the SEO, one can therefore expect a mean projected velocity of $\sim 2 \text{ km s}^{-1}$ or $\sim 4.2 \times 10^{-3} \text{ arcsec yr}^{-1}$. If the emitting volume covers a radial interval of $\Delta R \text{ arcsec}$ on the plane of the sky, the fraction lost per year is $(4.2 \times 10^{-3} / \Delta R) \times (1.0 \times 10^{-6}) \sim 4.2 \times 10^{-9} / \Delta R$ solar masses per Jy km s^{-1} of emission.

We explored different selection criteria to evaluate the total emission as well as different methods to evaluate the mass loss rate. As a result we estimate that an uncertainty of $\sim \pm 50\%$ is attached to the result. We present here two sets of selection criteria, which give total fluxes of 5.3 and 6.9 Jy km s^{-1} , respectively.

The first set selects a region in the central lower panel of Figure 7 defined as: $-1.7 < y' < -0.7$, $-1 < V_z - 2.5y'/4 < 1$, with y' in arcsec and V_z in km s^{-1} . The second selection is: $0.8 < R < 2 \text{ arcsec}$, $90^\circ < \omega < 180^\circ$, $-3 < V_z < 1 \text{ km s}^{-1}$.

Figure 9 displays intensity maps and Doppler velocity spectra for both selections. In each case, we evaluate $\Delta R \sim 1 \text{ arcsec}$. The mass loss rate is therefore evaluated as $(2.6 \pm 1.3) \times 10^{-8} \text{ M}_\odot \text{ yr}^{-1}$.

We see from Table 5 that the other main component of the current mass loss, the NEO, has a total flux of 6.7 Jy km s^{-1} . We estimate the values of its projected expansion velocity and ΔR

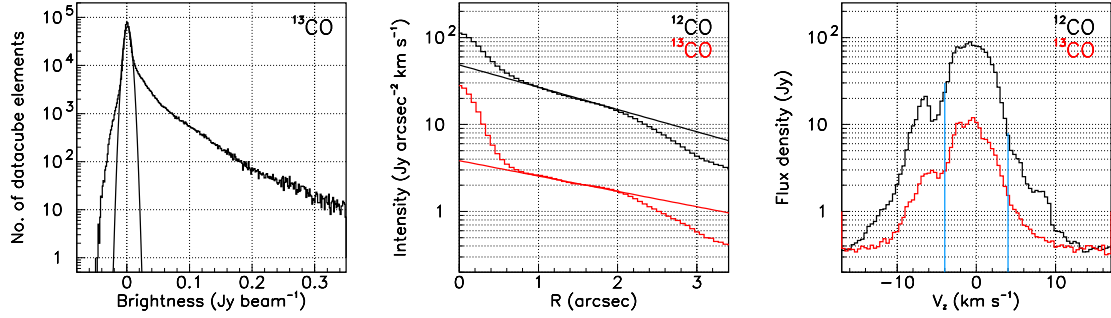


Figure 4. Left: brightness distribution of the $^{13}\text{CO}(3-2)$ emission measured over a data cube covering ± 3.7 arcsec in x and y and ± 10 km s $^{-1}$ in V_z . The curve is a Gaussian fit with a σ of 5 mJy beam $^{-1}$. Centre: radial distributions (after continuum subtraction) of the $^{12}\text{CO}(3-2)$ (black) and $^{13}\text{CO}(3-2)$ (red) emissions integrated over $|V_z| < 4$ km s $^{-1}$; the lines are exponential fits to the interval $1 < R < 2$ arcsec of the form $48 \exp(-R/1.7)$ and $3.9 \exp(-R/2.5)$ respectively. Right: Doppler velocity spectra of the $^{12}\text{CO}(3-2)$ (black) and $^{13}\text{CO}(3-2)$ (red) emissions integrated over $R < 3$ arcsec. The vertical lines show the interval considered in the present article, $|V_z| < 4$ km s $^{-1}$.

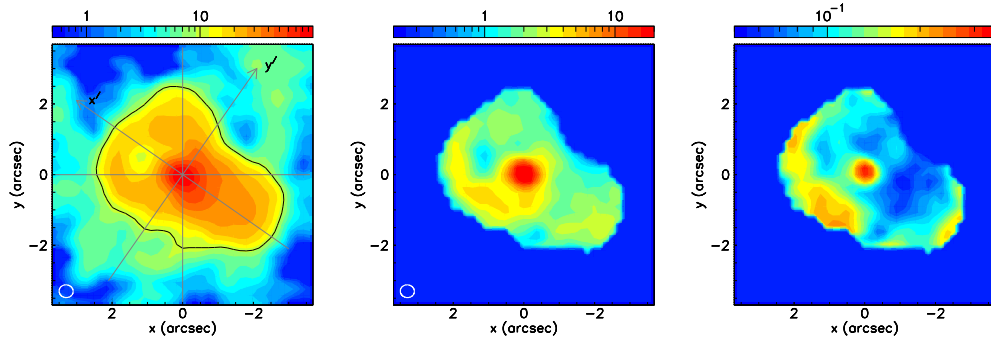


Figure 5. Left: map of the $^{12}\text{CO}(3-2)$ intensity (Jy km s $^{-1}$ arcsec $^{-2}$) integrated over $|V_z| < 4$ km s $^{-1}$. The black contour defines region C retained for the comparison between ^{12}CO and ^{13}CO emissions. The x' and y' axes are shown. Centre: map of the $^{13}\text{CO}(3-2)$ intensity (Jy km s $^{-1}$ arcsec $^{-2}$) in region C. Right: map of the $^{13}\text{CO}(3-2)/^{12}\text{CO}(3-2)$ intensity ratio in region C.

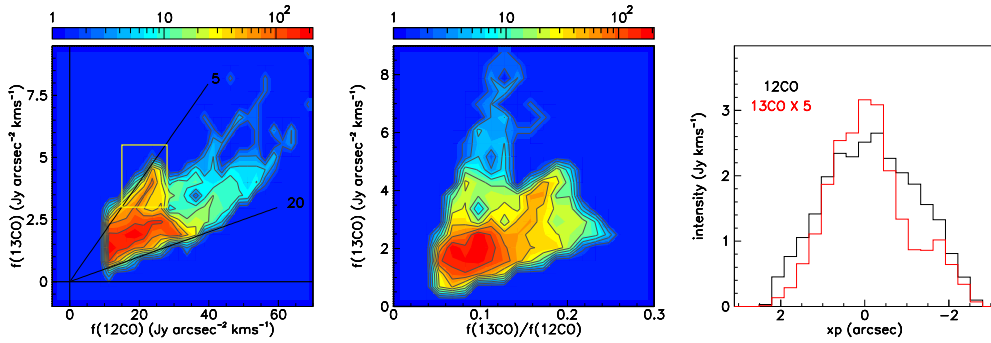


Figure 6. Left: intensities of $^{13}\text{CO}(3-2)$ emission vs $^{12}\text{CO}(3-2)$ emission measured in each pixel of region C. The yellow rectangle shows the distinctive feature discussed in the text. Centre: correlation in region C between the ^{13}CO intensity and the $^{13}\text{CO}/^{12}\text{CO}$ intensity ratio. Right: x' distribution of the intensities of the ^{12}CO and ^{13}CO emissions measured in the (V_z, y') region of the wind blowing toward Mira B.

Table 5. Compared emissions of the $^{12}\text{CO}(3-2)$ and $^{13}\text{CO}(3-2)$ lines in the fragments of region C. The last column lists the values for the SiO(5-4) emission with 3σ uncertainties (see Section 4).

| | x' (arcsec) | y' (arcsec) | V_z (km s $^{-1}$) | ^{12}CO (Jy km s $^{-1}$) | ^{13}CO (Jy km s $^{-1}$) | $^{13}\text{CO}/^{12}\text{CO}$ ratio | SiO(5-4) (Jy km s $^{-1}$) |
|-----|------------------|------------------|--------------------------|--|--|--|--------------------------------|
| NEA | >0.8 | - | >1.0 | 25 | 3.4 | 0.13 | 0.07 ± 0.10 |
| SWO | <-1.2 | - | >-1.0 | 65 | 6.5 | 0.10 | 11.2 ± 0.1 |
| NEO | >0.5 | - | <-1.3 | 45 | 6.7 | 0.15 | 0.65 ± 0.10 |
| SWS | - | >0.7 | <-1.5 | 29 | 3.7 | 0.13 | 4.65 ± 0.09 |
| SEO | - | $>-1.7, <-0.7$ | $>-3, <1$ | 54 | 8.2 | 0.15 | 0.88 ± 0.11 |

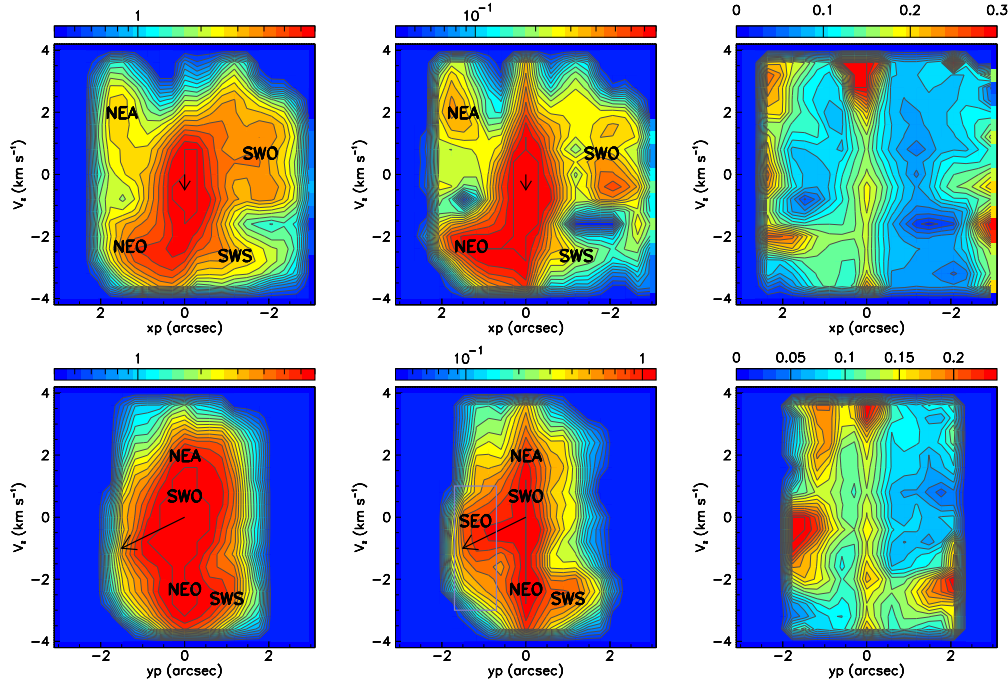


Figure 7. Comparing $^{12}\text{CO}(3-2)$ and $^{13}\text{CO}(3-2)$ emissions in region C: PV maps V_L vs x' (upper row) and vs y' (lower row). From left to right, $^{12}\text{CO}(3-2)$, $^{13}\text{CO}(3-2)$ and their ratio. The labels refer to the fragments defined in Table 5 of paper I and SWS stands for the newly identified south-western stream. NEA is for north-eastern arm, SWO for south-western outflow and NEO for north-eastern outflow; the arrow and the blue lines refer to the south-eastern outflow (SEO) dominated by the wind blowing from Mira A to Mira B. The color scales of the left and middle panels are in units of Jy.

to be both ~ 1.5 times larger than for the SEO, meaning a same contribution to the mass loss rate. Adding a contribution from the SWS and possibly from a small remaining flow from the SWO, evaluated at the same level as those of SEO and NEO gives a total mass loss rate of $\sim (8 \pm 4) \times 10^{-8} M_{\odot} \text{yr}^{-1}$. While crude, this evaluation is the result of a direct measurement and is therefore more reliable than the indirect estimates usually quoted (see Table 1), which are typically 5 times larger.

In summary, the present section has given evidence for ongoing mass-loss from the central volume of high density gas previously identified by recent studies (e.g. Khouri et al. 2018) to the blue shifted hemisphere in three preferred directions: two outflows, SEO and NEO, the former being dominated by wind blowing toward, and focused by Mira B, and a smaller flow that had been included in the south-western outflow in paper I and which we refer to as SWS. Together, they add up to a total mass loss rate of $\sim (8 \pm 4) \times 10^{-8} M_{\odot} \text{yr}^{-1}$. In addition, two major fragments emitted a few decades ago, the NEA and the SWO, which had also been identified and studied in paper I, have been shown to be nearly detached from the central reservoir and to give further evidence for the episodic nature of the mass loss of Mira A. A detailed study of the $^{13}\text{CO}(3-2)$ emission has shown the broad range covered by the measured intensity ratio $^{13}\text{CO}(3-2)/^{12}\text{CO}(3-2)$, compatible with the expected effect of absorption and confirming the results of the brief analysis presented in paper I, with a mean measured $^{13}\text{CO}/^{12}\text{CO}$ intensity ratio of 0.14, corresponding to a $^{12}\text{CO}/^{13}\text{CO}$ abundance ratio of 12 ± 2 after correction for absorption and accounting for the slightly different excitation parameters.

4 PECULIAR MORPHOLOGY OF THE SIO(5-4) EMISSION

The abrupt decline of SiO emission beyond some 6 au from the centre of Mira A was first noticed by Wong et al. (2016). In this context, we note that the Doppler velocity spectrum observed over the stellar disc usually shows, in addition to absorption in the inner layers of the CSE, a relatively narrow blue-shifted spike that signals the terminal velocity in the outer layers of the CSE, observed along the line of sight crossing the star in its centre. In the case of Mira A, no such spike is visible. Khouri et al. (2018, 2019) have shown that similar confinements affect the emissions of the $\text{SO}(N_J = 8_8 - 7_7)$, $^{13}\text{CO}(3-2)$, $\text{CO}(\nu=1,3-2)$ and $\text{AlO}(N=9-8)$, as well as other molecular line emissions, with dust clustering on the northern and north-western edges of the region of SO emission, beyond some 8 au north from the star centre. In the preceding section, we have shown that the present observations of the emission of the $\text{CO}(3-2)$ line was also consistent with such a confinement for both isotopologues. Figure 10 compares intensity maps of these emissions, including the emission of the SiO(5-4) line obtained from the same data as analysed in Section 2. In the present section, we revisit the analysis of the latter with the aim to review critically the conclusions presented in paper I. Indeed, these observations are challenging in at least two respects: the absence of SiO emission over most of the sky plane is at strong variance with what we know of other oxygen-rich AGB stars; its presence in a small south-western region needs therefore to be explained, paying particular attention to significant differences displayed there by CO and SiO emissions.

The episodic nature of the mass loss evidenced in the preceding section implies that it is difficult to escape the gravity of Mira A+B (~ 2.7 solar masses). Indeed, at 15 au from the centre of the star, the escape velocity from Mira A is 15.4 km s^{-1} , larger than the boost that the shocks induced by pulsations and convective cell ejections

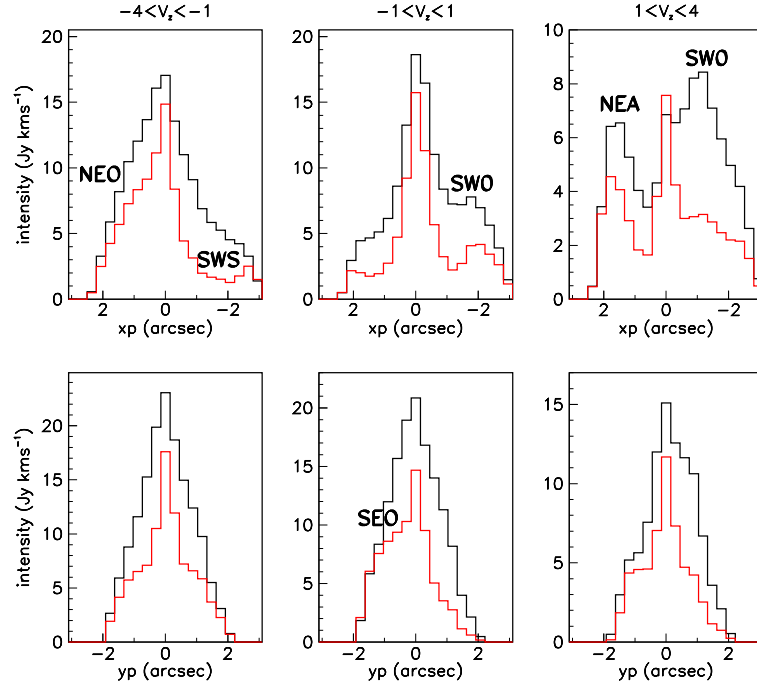


Figure 8. Projections of the intensities in region C of the ¹²CO(3-2) (black) and ¹³CO(3-2) (red, multiplied by 5) emissions on the x' axis (upper row) and the y' axis (lower row). In each panel, three separate intervals of Doppler velocity are considered as indicated on top.

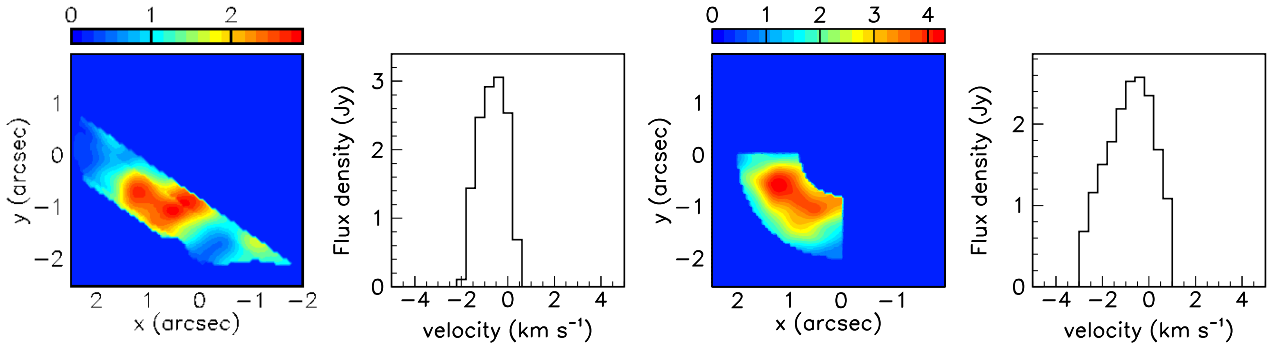


Figure 9. Intensity maps and Doppler velocity spectra of the two selections used to evaluate the mass loss rate in the south-eastern quadrant (see text). The color scales are in units of Jy arcsec⁻² km s⁻¹.

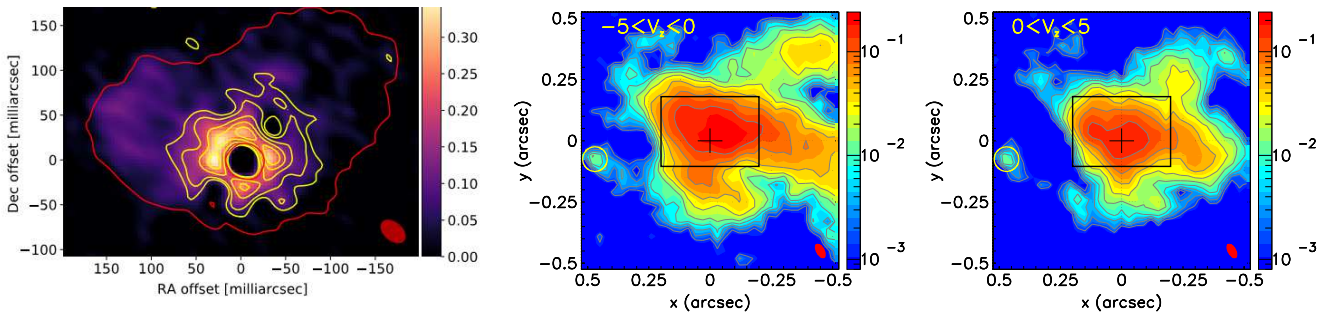


Figure 10. Left: Figure 8 of Khouiri et al. (2018), comparing the emissions of AlO($N=9-8$), SO($N_J = 8_8 - 7_7$) (red contour) and CO($v=1,3-2$) (yellow contours). Dust covers the northern part of the SO emission region, beyond some 80 mas north of the star. Centre and right: intensity maps of the SiO(5-4) emission integrated in the blue (centre) and red (right) hemispheres respectively. The location of Mira B, revealed by its continuum emission, is indicated by a yellow circle. The color scales are in units of Jy beam⁻¹ km s⁻¹.

usually produce. Beyond this distance, these shocks are no longer playing a role in the generation of the nascent wind. The presence of a wind, with matter escaping the gravity of Mira A+B, relies therefore fully on whatever acceleration mechanism is at stake to follow up on the original boost. The complexity of the mechanisms which we know about, essentially collisions with dust grains to which the UV radiation of the star transfers momentum, is such that we cannot hope for accurate predictions. As was emphasized by [Woitke \(2006\)](#) fifteen years ago, oxygen-rich stars, in strong contrast with carbon-rich stars, are not good at producing dust grains that can efficiently accelerate the wind. The physico-chemistry at stake depends on the size and nature of the dust grains, on the nature and the rate of their formation, on their temperature, on how refractory and transparent they are, all of which can take a broad range of values. Of similar relevance is the model developed by [Winters et al. \(2000\)](#), which predicts the existence of a class of low mass loss rate AGB stars for which the acceleration is essentially caused by the boost given by pulsations, the dust paying only a secondary role.

Qualitatively, these considerations are good candidates to explain both the confinement of a large gas density at short distance from the star and the episodic and anisotropic nature of the mass loss: to a first approximation, there is simply no mass loss and gas accumulates around the star; to a second approximation mass loss occurs wherever and whenever there is a weak point through which matter can leak, causing episodic and anisotropic mass loss. In particular mass loss may permanently proceed toward Mira B in the direction of the gravity gradient. Quantitatively, however, these arguments fail to account for several puzzling features displayed by the SiO(5-4) emission.

4.1 Reliability of the SiO emission image

Among such puzzling features are the different morphologies displayed by CO and SiO emissions in the south-western quadrant. Their study requires, as a preliminary, to ascertain the validity of the imaging process: possible artefacts and/or significant distortions must be identified before attempting any sensible interpretation. In particular, the SiO observations were obtained with a very different and much more extended antenna configuration than the CO observations: the radial extent over which they are reliable needs to be carefully examined. The left panel of Figure 11 displays the baseline distribution of the antenna configuration used for the SiO observations. In order to assess the effect of the depression observed around $\sim 550 \pm 250$ m, we produce visibilities using an isotropic wind as a source and image the result. The radial distribution of the imaged intensity, which is constant at a level of ~ 53 mJy for the source, is shown in the central-left panel of Figure 11. The imaging is found to be generally well behaved, with oscillations not exceeding $\pm 20\%$. As the wavelength is 1.38 mm, the depression of the baseline distribution corresponds to angular distances of 0.62 ± 0.27 arcsec. At variance with similar observations of W Hya ([Hoai et al. 2021](#)), where the baseline distribution displays a similar but deeper depression, the distortion observed in this region is not strong: the central region of the uv map (baselines smaller than ~ 500 m) is sufficiently and adequately covered by the antenna configuration. As a further check, we use as a source, instead of an isotropic wind, the intensity map of the $^{13}\text{CO}(3-2)$ emission restricted to the region ($-1 < V_z < 2$ km s $^{-1}$, $x' < 1$ arcsec) where the bulk of the emission takes place; we again produce visibilities using the antenna configuration of the SiO observations and reconstruct the image. The result is displayed in the central-right panel of Figure 11 and the radial distributions of the intensity of source and image, integrated over position angles,

are compared in the right panel. Imaging is again found to be well behaved up to distances of at least 3 arcsec from the star; small differences are observed but they are much too small to be of concern for the very strong effects that we are after, and which we study in the next sections.

4.2 Confinement at short distances of the SiO emissions outside the south-western quadrant

Figure 10 shows that Mira A is currently ejecting SiO gas molecules mostly toward the blue hemisphere, as it does for CO molecules. However, closer inspection reveals major differences between the two emissions. This is illustrated in Figure 12, which compares PV maps of V_z vs x' and y' for the emission of ^{13}CO and SiO molecules as was done in Figure 7 for the two CO isotopologues. The comparison is made with ^{13}CO rather than ^{12}CO in order to minimize effects of absorption. SiO is essentially absent from the SEO, the NEA and the NEO but is present in the SWO and the SWS. The last column of Table 5 lists the values of the measured intensities; they are a bit larger than the $^{13}\text{CO}(3-2)$ intensities for SWO and SWS but an order of magnitude smaller for NEA, NEO and SEO. The above considerations on the difficulty to escape the Mira A+B gravity fail to explain this feature.

To get deeper insight into the lack of SiO emission in most of the sky plane, we exclude the south-western quadrant from the remaining of the present section and keep its study for the next section. For the values of SiO emission listed in Table 5 to be meaningful, the identification of each fragment in terms of intervals of x' , y' and V_z must properly match both CO and SiO observations: is SiO completely absent outside the south-western quadrant or is it present in each CO fragment, but at a much lower level? We explored this issue in considerable details and concluded in favour of the latter. We illustrate it in the case of the NEA in Figure 13. We choose NEA because it is most clearly identified in CO emission and because the value quoted in Table 5 is compatible with noise. We first identify the NEA from the CO emission displayed in Figure 7 in stricter terms than done in Table 5: $1 < x' < 2$ arcsec and $1 < V_z < 4$ km s $^{-1}$; we then plot, for this selection of x' and V_z , the PV maps (V_z vs ω). While being an order of magnitude smaller than the CO intensity (0.23 vs 2.68 Jy km s $^{-1}$) the SiO intensity displays an ω distribution clearly correlated with that of the CO intensity.

In the optically thin approximation, the ratio between the SiO and ^{13}CO column densities associated with a same emissivity is $\sim 7.5 \cdot 10^{-3}$. Assuming a typical SiO/ ^{13}CO intensity ratio of ~ 0.1 outside the south-western quadrant and a $^{12}\text{CO}/^{13}\text{CO}$ abundance ratio of 12 (temperature is nearly irrelevant) gives an SiO/CO abundance ratio of $6.3 \cdot 10^{-5}$. Excluding the south-western quadrant, the episodic mass loss of Mira A produces therefore fragments containing both SiO and ^{12}CO molecules, the latter being typically 1 to $2 \cdot 10^4$ times more abundant than the former.

In general, the SiO abundance of the wind of oxygen-rich AGB stars decreases progressively when the distance from the star increases, a result of the condensation of the gas on dust grains ([Schöier et al. 2004](#)) before being dissociated by the UV interstellar radiation at a few 100 au from the star. Figure 14 illustrates the specificity of Mira A in this context by comparing the radial dependence of the SiO and CO intensities between Mira A, EP Aqr and R Dor. For the comparison to be meaningful, we measure R in units of au and the line emissions are scaled to SiO(5-4) and CO(3-2) using parameters listed in Table 6 and assuming a radial dependence of the temperature of the form $T[\text{K}] = 100/R[\text{arcsec}]$. At a projected distance of 100 au from the centre of the star, the SiO/CO ratio is over

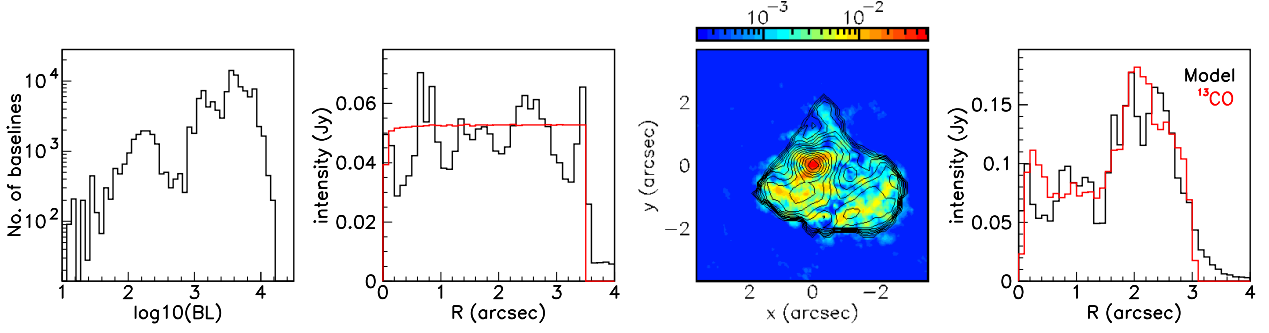


Figure 11. Left: baseline distribution of the antenna configuration used for the observation of the SiO(5-4) emission. Centre-left: radial distribution of the imaged intensity of an isotropic wind of constant intensity (~ 53 mJy). The red line is for the source. Centre-right: image (colour) obtained using as source the ^{13}CO emission (contours) in the south-western quadrant (see text). Right: comparison between source and model radial distributions using as source the ^{13}CO emission.

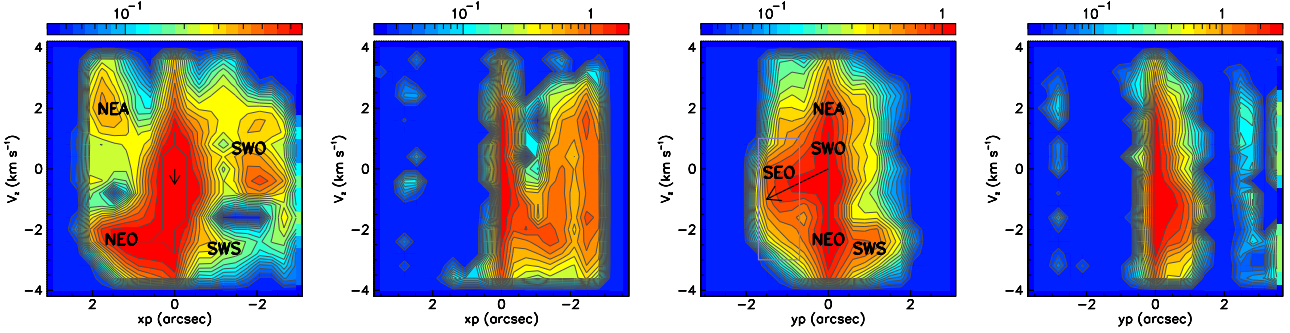


Figure 12. Comparing $^{13}\text{CO}(3-2)$ and SiO emissions: PV maps V_z vs x' (left pair) and vs y' (right pair). In each pair of panels $^{13}\text{CO}(3-2)$ is left and SiO(5-4) is right. The labels are the same as defined in Figure 7. CO emission is from region C only but SiO emission is not restricted to a particular region. The color scales are in units of Jy.

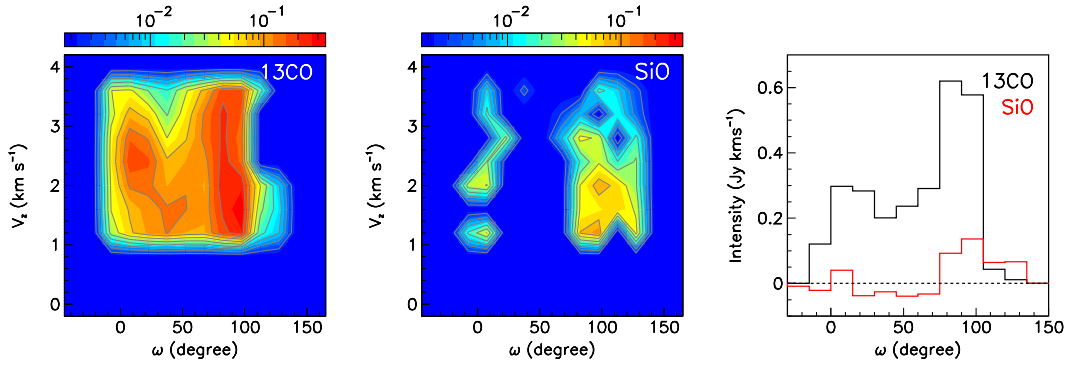


Figure 13. Comparison of the NEA intensities observed in $^{13}\text{CO}(3-2)$ and SiO(5-4) emissions. PV maps are shown in the left (^{13}CO) and central (SiO) panels. The ω distributions are shown in the right panel. The color scales are in units of Jy.

two orders of magnitude smaller in Mira A than in R Dor and EP Aqr. The SiO emission of the CSEs of other low mass-loss-rate oxygen-rich AGB stars, such as W Hya (Takigawa et al. 2017; Hoai et al. 2021), RS Cnc (Winters et al. 2021), R Leo (Fonfría et al. 2019a,b), R Hya (Homan et al. 2021) has also been observed at ALMA; in general, the SiO emission, while being significantly more compact than the CO emission, extends beyond 150 au, providing additional evidence for the specificity of Mira Ceti.

The distributions displayed in Figure 14 cover the whole sky, the south-western quadrant has not been excluded and its contribution in Mira Ceti is clearly visible beyond ~ 50 au. In order to obtain

an evaluation of the SiO/CO intensity ratio outside the south-western quadrant, independent from the value ~ 0.1 estimated from Table 5, we display in Figure 15 the intensity map of the SiO emission and its radial distribution for various intervals of position angles. Beyond 100 au from the star, excluding the south-western quadrant, the SiO intensity is at the $0.1 \text{ Jy arcsec}^{-2} \text{ km s}^{-1}$ level, while the CO intensity is $\sim 20 \text{ Jy arcsec}^{-2} \text{ km s}^{-1}$. The ratio between the SiO and ^{13}CO intensities beyond 100 au and excluding the south-western quadrant is therefore ~ 0.05 , consistent with our 0.1 estimate from Table 5.

In summary, we can state with confidence that the abundance

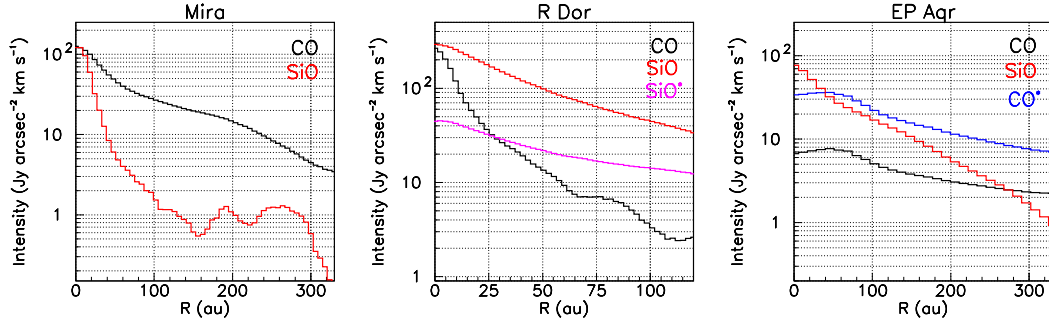


Figure 14. Comparing the radial dependence of SiO and CO emissions between Mira A, R Dor and EP Aqr. Details of relevance are listed in Table 6. The starred histograms have been corrected for the different line excitations and correspond to SiO(5-4) and CO(3-2). Note the different R scale for R Dor.

ratio between SiO and ^{12}CO , excluding the south-western quadrant, is at the level of $(0.5 \text{ to } 1) \times 10^{-4}$.

We explored several scenarios that might explain the very low SiO/CO ratio observed beyond some 50 au from the star. Of course, SiO molecules are 57% more massive than CO molecules, and it takes therefore 57% more energy to free them from the gravity of Mira A+B; however, this argument is supposed to be irrelevant: hydrodynamical models show that the gas velocity is essentially locked to the dust grain velocity, independently from the mass of the molecules. Similarly, the temperature is not expected to play any significant role, the upper level energies being nearly the same: 31.7 K for $^{13}\text{CO}(3-2)$ and 31.3 K for SiO(5-4). Dissociation of the SiO molecules by UV radiation, either from Mira A, Mira B or the ISM, could play a role: one might claim to see the effect of dissociation from Mira B radiation in the central panel of Figure 9 (the emission of Mira B itself is from the continuum); but the radiations from Mira A and B should have no effect on distant fragments such as the NEA. However, the overall low density of the Mira CSE beyond ~ 50 au is certainly enhancing the dissociation of the SiO molecules by the ISM radiation. Finally, the most likely scenario is that nearly all SiO molecules have condensed onto dust grains before escaping the Mira A+B gravity (at 50 au from the star, the escape velocity from Mira A is still $\sim 9 \text{ km s}^{-1}$). Assessing the likelihood of such a scenario implies a detailed understanding of the process of dust formation, probably deeper than what current knowledge can offer. It is the scenario retained in paper I as interpretation of the south-western emission of the SiO line.

4.3 Different emissions of the CO and SiO lines in the south-western quadrant

In paper I, we studied in detail the south-western region that includes the fragments SWO and SWS of the present study. In the present section we extend the analysis to a comparison between the SiO(5-4) and $^{13}\text{CO}(3-2)$ emissions, which is more free of absorption effects than the SiO(5-4) vs $^{12}\text{CO}(3-2)$ comparison presented in paper I. Figure 16 displays PV maps (V_z vs ω) in two intervals of R separately: $1 < R < 2$ arcsec and $2 < R < 3$ arcsec. At first glance, CO and SiO emissions seem to be completely unrelated. Essentially, SiO emission reveals a flow covering $V_z = -1.7 \pm 0.7 \text{ km s}^{-1}$ and $\omega = 265^\circ \pm 15^\circ$ for R between 1 and 2 arcsec and a broad area covering $|V_z| < 4 \text{ km s}^{-1}$ and $\omega = 250^\circ \pm 30^\circ$ for R between 2 and 3 arcsec. Paper I refers to these as first and second components of SiO emission, respectively. CO emission covers the whole south-western quadrant but is strongly depressed toward the west at $V_z \sim -1.5 \pm 0.5 \text{ km s}^{-1}$.

In paper I, we speculated that a mass ejection associated with

the 2003 X-ray burst and centred on the first SiO component has been punching a hole through the CO volume at a velocity of some 130 km s^{-1} to reach $R \sim 3$ arcsec in 2014. We note that the dates of observation were only 4.5 months apart: 12-15 June for CO and 1st November for SiO, during which time the mass ejection and associated shock wave would have covered ~ 10 au. The mass ejection left accordingly a low density wake behind it, and is assumed to have been accompanied by a shock front that caused the SiO molecules trapped in dust grains to outgas. We do not repeat here the details of the argumentation but in spite of its speculative nature this scenario accounts well, at least qualitatively, for the main observed features of both SiO and CO emissions. Figure 17 extends Figure 7 of paper I to ^{13}CO emission and Figure 18 displays the radial profiles of the SiO, ^{12}CO and ^{13}CO emissions; together with Figure 16, they illustrate well the relevant features of the morpho-kinematics. Accepting this interpretation would require a quantitative modelling of the event, which is well beyond the scope of the present article. We retain however that such a scenario has the advantage of decoupling the mechanisms of the disturbance caused by the mass ejection from that of generation of the nascent wind, in which we are interested. It is consistent with the latter being described as episodic mass loss in the form of fragments strongly depleted of SiO molecules, with a SiO/CO abundance ratio at the level of $0.5 \text{ to } 1 \times 10^{-4}$: the whole SiO emission is interpreted as due to SiO molecules, which outgassed, eleven years before the observation, from dust grains present in the pre-existing SWO.

We studied in considerable details the anti-correlation displayed by the CO(3-2) and SiO(5-4) emissions in the south-western quadrant but failed to find another sensible interpretation than proposed in paper I. If true, this interpretation has the merit of having significantly unravelled the complexity of the observed morpho-kinematics: models aiming at a description of the genesis of the wind of Mira A should simply ignore the south-western quadrant.

5 SUMMARY AND CONCLUSION

We have revisited, and extended to $^{13}\text{CO}(3-2)$ emission, a number of analyses of the morpho-kinematics of the nascent wind of Mira A presented in paper I, in the light of current knowledge of its main features.

Some results have strengthened and confirmed earlier results. These include:

- the broad line width displayed by the SiO(5-4) emission at distances from the star between 5 and 15 au, evidence for the impor-

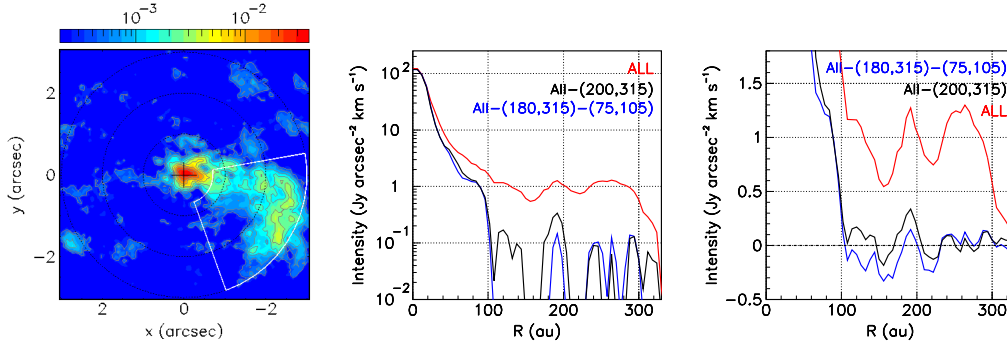


Figure 15. Left: Intensity ($\text{Jy arcsec}^{-2} \text{ km s}^{-1}$) map of SiO(5-4) emission integrated in the $|V_z| < 4 \text{ km s}^{-1}$ interval. Centre and right: radial distribution of the intensity mapped in the left panel for different intervals of position angles, as listed in the inserts. The central panel is in log scale and the right panel in linear scale in order to show the noise level.

Table 6. Parameters of relevance to the comparison presented in Figure 14.

| | Mira (this work) | | R Dor (Nhung et al. 2021) | | EP Aqr (Tuan-Anh et al. 2019) | |
|---|-----------------------|----------------------|------------------------------|-----------------------|----------------------------------|----------------------|
| D (pc) | 100 | | 60 | | 114 | |
| Line | CO(3-2) | SiO(5-4) | CO(3-2) | SiO(8-7) | CO(2-1) | SiO(5-4) |
| Beam (arcsec^2) | 0.39×0.36 | 0.06×0.03 | 0.18×0.14 | 0.22×0.17 | 0.33×0.30 | 0.29×0.25 |
| Frequency (GHz) | 345.8 | 217.1 | 345.8 | 347.3 | 230.5 | 217.1 |
| Noise (σ , mJy beam^{-1}) | 14 | 0.66 | 14 | 18 | 6 | 3.9 |
| Einstein coef. A_{ji} (s^{-1}) | 2.50×10^{-6} | 5.2×10^{-4} | 2.50×10^{-6} | 22.0×10^{-4} | 6.91×10^{-7} | 5.2×10^{-4} |
| Upper level E_u (K) | 33.2 | 31.3 | 33.2 | 75.0 | 16.6 | 31.3 |

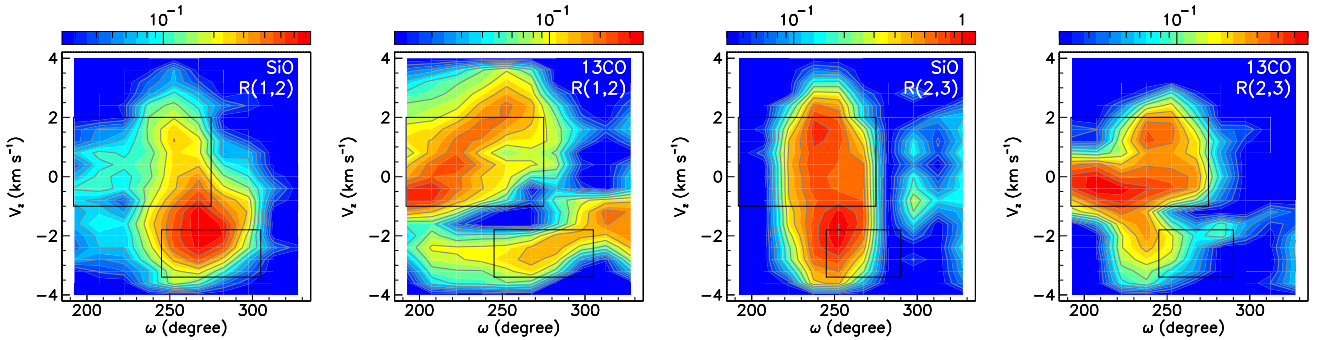


Figure 16. PV maps (V_z vs ω) of SiO(5-4) and $^{13}\text{CO}(3-2)$ emissions in the south-western region. The first two panels are integrated over $1 < R < 2$ arcsec, the last two over $2 < R < 3$ arcsec. In each pair, SiO is left and ^{13}CO is right. The large rectangles indicate the location of the SWO fragment and the small rectangles of the SWS fragment as defined from Figure 12. The color scales are in units of Jy.

tance of shocks induced by pulsations and convective cell ejections as abundantly revealed by observations at shorter wavelengths;

- the confinement of a high density gas volume around the star, again abundantly evidenced by observations at shorter wavelengths such as by Khouri et al. (2018);

- increased support to the scenario presented in paper I to explain the presence of SiO emission in the south-western quadrant.

Some have presented new results. These include:

- the possible presence of rotation about an axis projecting $40^\circ \pm 15^\circ$ east of north with a projected velocity of $0.7 \pm 0.2 \text{ km s}^{-1}$, in agreement with results obtained from the observation of SiO masers;

- the presence of two fragments, SWO and NEA, emitted a few decades ago and nearly detached from the central gas reservoir, giving additional evidence for the episodic nature of the mass loss;

- the current mass loss proceeding toward the blue hemisphere

along three favoured directions: the SEO, dominated by the wind focused by Mira B, the NEO and the SWS;

- a detailed exploration of the $^{13}\text{CO}(3-2)$ emission revealing absorption in the $^{12}\text{CO}(3-2)$ emission and essentially confirming the results presented in paper I;

- a critical study of the reliability of the imaging process of the SiO(5-4) emission;

- an evaluation of the current mass loss rate as $\sim (8 \pm 4) \times 10^{-8} \text{ M}_\odot \text{ yr}^{-1}$, much smaller than usually assumed;

- a detailed study of the suppression of SiO abundance beyond the central high density gas volume, and a comparison with other AGB stars;

- an evaluation of the SiO/CO abundance ratio at the level of 0.5 to 1×10^{-4} when excluding the south-western quadrant, at least two orders of magnitude smaller than other typical low mass-loss-rate oxygen-rich AGB stars.

The main contribution of the present work to our understand-

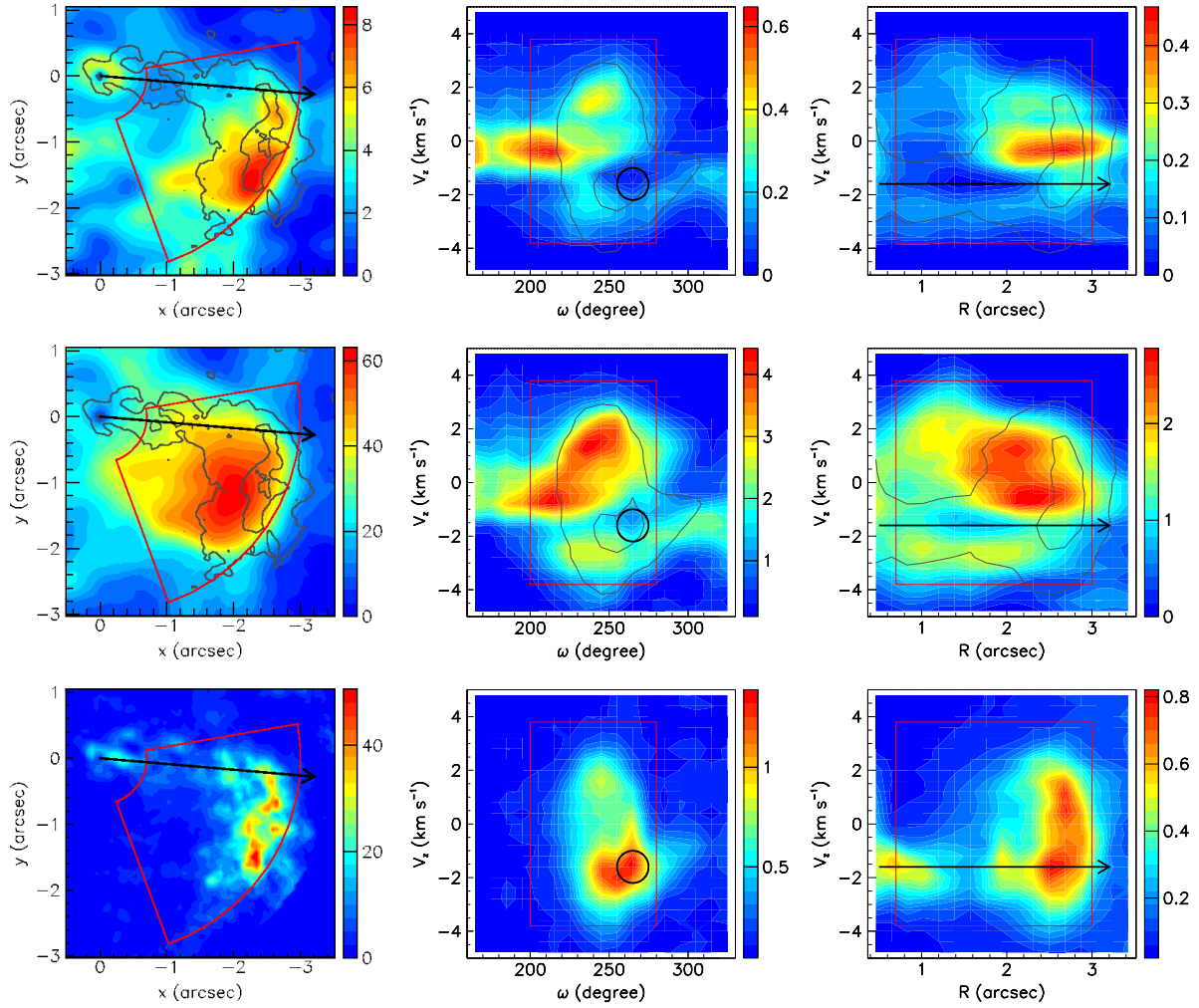


Figure 17. Projections of the south-western region of the data cube delimited by red lines, on the (x, y) plane (left, multiplied by R), the (V_z, ω) plane (centre) and the (V_z, R) plane (right). Units for the left panels are $\text{Jy arcsec}^{-1} \text{ km s}^{-1}$ and for the other panels Jy . From up down, ^{13}CO , ^{12}CO and SiO emissions. SiO contours are superimposed on the CO panels. The arrows and circles indicate the supposed trajectory of the 2003 mass ejection. The ^{12}CO and SiO panels were reproduced from Figure 7 of paper I.

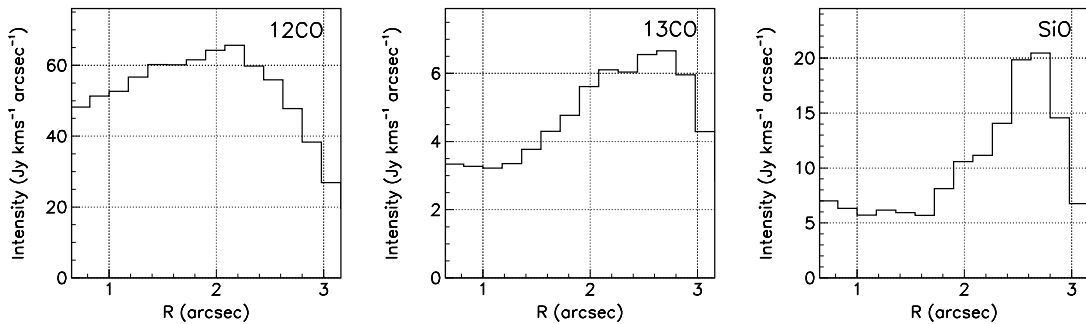


Figure 18. Radial profiles of SiO , ^{13}CO and ^{12}CO emissions integrated in the region defined in Figure 17.

ing of the wind of Mira Ceti has been to reduce the problem to explaining why and how the mass loss is episodic and takes the form of fragments having an SiO/CO abundance ratio much lower than usual. Here episodic should not be understood in too radical a way: we deal with modulations of the mass loss rate over periods

of several decades with peak-to-valley ratios of a few, no more than an order of magnitude. Moreover, we note that the north-east/south-west direction seems to be a preferred direction for the outflows; a probably permanent component of the wind is the part focused by Mira B, but the direction of the flow evolves slowly, at the pace of

the orbital period, some 500 years. We have presented hand-waving arguments in favour of such features, noting the difficulty for the atmosphere of an oxygen-rich AGB star to escape the gravity of the 2.7 solar masses A+B pair. Similar arguments were used by Winters et al. (2000) in predicting the existence of a class of very low mass loss rate AGB stars where pulsations rather than dust play the main role in accelerating the wind. The picture that results suggests that small perturbations to the zero-order picture where there is simply no mass loss are sufficient to trigger episodes of fragmentary loss. To quantitatively support such arguments requires a detailed modelling of the dust-gas chemistry at stake, probably well beyond what current models can address (see Section 1.2).

The present results cannot be ignored by hydro-dynamical and physico-chemical models attempting a description of the nascent wind. Indeed, if Mira A is an archetype in terms of its variability, it is rather atypical in terms of the generation of its wind. Such models can be expected to find it very difficult to account for its peculiar features, small variations in the parameters deciding when and where mass loss can proceed significantly. Lower mass AGB stars, with mass loss rates at a few $10^{-7} \text{ M}_{\odot} \text{ yr}^{-1}$, and preferably without known companion, are probably a better choice for them to develop.

ACKNOWLEDGEMENTS

We thank Professors J. Alcolea, B. Freytag, T. Khouri, G. Perrin, and K.T. Wong for having helped us to better understand Mira by answering and/or clarifying questions we had concerning both their work and the general picture. This paper uses ALMA data ADS/JAO.ALMA#2011.0.00014.SV and ADS/JAO.ALMA#2013.1.00047.S. ALMA is a partnership of ESO (representing its member states), NSF (USA) and NINS (Japan), together with NRC (Canada), MOST and ASIAA (Taiwan), and KASI (Republic of Korea), in cooperation with the Republic of Chile. The Joint ALMA Observatory is operated by ESO, AUI/NRAO and NAOJ. The data are retrieved from the JVO/NAOJ portal. We are deeply indebted to the ALMA partnership, whose open access policy means invaluable support and encouragement for Vietnamese astrophysics. Financial support from the World Laboratory, the Odon Vallet Foundation and VNSC is gratefully acknowledged. This research is funded by the Vietnam National Foundation for Science and Technology Development (NAFOSTED) under grant number 103.99-2019.368.

REFERENCES

- Chandler A. A., Tatebe K., Wishnow E. H., Hale D. D. S., Townes C. H., 2007, *ApJ*, **670**, 1347
- Cotton W. D., et al., 2004, *A&A*, **414**, 275
- Cotton W. D., et al., 2006, *A&A*, **456**, 339
- De Vicente P., et al., 2016, *A&A*, **589**, A74
- Decin L., Richards A. M. S., Danilovich T., Homan W., Nuth J. A., 2018, *A&A*, **615**, A28
- Fonfría J. P., Santander-García M., Cernicharo J., Velilla-Prieto L., Agúndez M., Marcelino N., Quintana-Lacaci G., 2019a, in *ALMA2019: Science Results and Cross-Facility Synergies*. p. 85, doi:10.5281/zenodo.3585368
- Fonfría J. P., Santander-García M., Cernicharo J., Velilla-Prieto L., Agúndez M., Marcelino N., Quintana-Lacaci G., 2019b, *A&A*, **622**, L14
- Haniff C. A., Scholz M., Tuthill P. G., 1995, *MNRAS*, **276**, 640
- Heras A. M., Hony S., 2005, *A&A*, **439**, 171
- Hoai D. T., Tuan-Anh P., Nhung P. T., Darriulat P., Diep P. N., Phuong N. T., Thai T. T., 2020, *MNRAS*, **495**, 943
- Hoai D. T., Nhung P. T., Tuan-Anh P., Darriulat P., Diep P. N., Ngoc N. T. B., Thai T. T., 2021, *MNRAS*, submitted
- Homan W., et al., 2021, *A&A*, **651**, A82
- Ireland M. J., et al., 2007, *ApJ*, **662**, 651
- Kamiński T., et al., 2016, *A&A*, **592**, A42
- Kamiński T., et al., 2017, *A&A*, **599**, A59
- Karovska M., Hack W., Raymond J., Guinan E., 1997, *ApJ*, **482**, L175
- Karovska M., Schlegel E., Hack W., Raymond J. C., Wood B. E., 2005, *ApJ*, **623**, L137
- Khoury T., Vlemmings W. H. T., Ramstedt S., Lombaert R., Maercker M., De Beck E., 2016, *MNRAS*, **463**, L74
- Khoury T., Vlemmings W. H. T., Olofsson H., Ginski C., De Beck E., Maercker M., Ramstedt S., 2018, *A&A*, **620**, A75
- Khoury T., Vlemmings W. H. T., Olofsson H., Ginski C., De Beck E., Maercker M., Ramstedt S., 2019, *IAU Symposium*, **343**, 31
- Kipper T., 1992, *Baltic Astronomy*, **1**, 190
- Martin D. C., et al., 2007, *Nature*, **448**, 780
- Matthews L. D., Karovska M., 2006, *ApJ*, **637**, L49
- Matthews L. D., Reid M. J., Menten K. M., 2015, *ApJ*, **808**, 36
- Mayer A., et al., 2011, *A&A*, **531**, L4
- Meaburn J., López J. A., Boumis P., Lloyd M., Redman M. P., 2009, *A&A*, **500**, 827
- Montez Rodolfo J., Ramstedt S., Kastner J. H., Vlemmings W., Sanchez E., 2017, *ApJ*, **841**, 33
- Nhung P. T., Hoai D. T., Diep P. N., Phuong N. T., Thao N. T., Tuan-Anh P., Darriulat P., 2016, *MNRAS*, **460**, 673
- Nhung P. T., Hoai D. T., Tuan-Anh P., Darriulat P., Diep P. N., Ngoc N. B., Phuong N. T., Thai T. T., 2021, *MNRAS*, **504**, 2687
- Perrin G., et al., 2020, *A&A*, **642**, A82
- Planesas P., Alcolea J., Bachiller R., 2016, *A&A*, **586**, A69
- Prieur J. L., Aristidi E., Lopez B., Scardia M., Mignard F., Carbillet M., 2002, *ApJS*, **139**, 249
- Ramstedt S., et al., 2014, *A&A*, **570**, L14
- Reimers D., Cassatella A., 1985, *ApJ*, **297**, 275
- Ryde N., Schöier F. L., 2001, *ApJ*, **547**, 384
- Schöier F. L., Olofsson H., Wong T., Lindqvist M., Kerschbaum F., 2004, *A&A*, **422**, 651
- Skiff B. A., 2014, *yCat*, **1**, 2023
- Sokoloski J. L., Bildsten L., 2010, *ApJ*, **723**, 1188
- Takigawa A., Kamizuka T., Tachibana S., Yamamura I., 2017, *Science Advances*, **3**, eaao2149
- Templeton M. R., Karovska M., 2009, *ApJ*, **691**, 1470
- Thirumalai A., Heyl J. S., 2013, *MNRAS*, **430**, 1359
- Tuan-Anh P., et al., 2019, *MNRAS*, **487**, 622
- Ueta T., 2008, *ApJ*, **687**, L33
- Vanture A. D., Wallerstein G., Brown J. A., Bazan G., 1991, in *Bulletin of the American Astronomical Society*. p. 966
- Vlemmings W. H. T., Ramstedt S., O’Gorman E., Humphreys E. M. L., Wittkowski M., Baudry A., Karovska M., 2015, *A&A*, **577**, L4
- Vlemmings W. H. T., Khoury T., Olofsson H., 2019, *A&A*, **626**, A81
- Winters J. M., Le Bertre T., Jeong K. S., Helling C., Sedlmayr E., 2000, *A&A*, **361**, 641
- Winters J. M., Le Bertre T., Jeong K. S., Nyman L. Å., Epchtein N., 2003, *A&A*, **409**, 715
- Winters J. M., et al., 2021, *A&A*, submitted
- Wittkowski M., Chiavassa A., Freytag B., Scholz M., Höfner S., Karovicova I., Whitelock P. A., 2016, *A&A*, **587**, A12
- Woitke P., 2006, *A&A*, **460**, L9
- Wong K. T., Kamiński T., Menten K. M., Wyrowski F., 2016, *A&A*, **590**, A127
- Wood B. E., Karovska M., 2006, *ApJ*, **649**, 410
- Wood B. E., Karovska M., Raymond J. C., 2002, *ApJ*, **575**, 1057
- Woodruff H. C., et al., 2004, *A&A*, **421**, 703
- van Leeuwen F., 2007, *A&A*, **474**, 653

APPENDIX A:

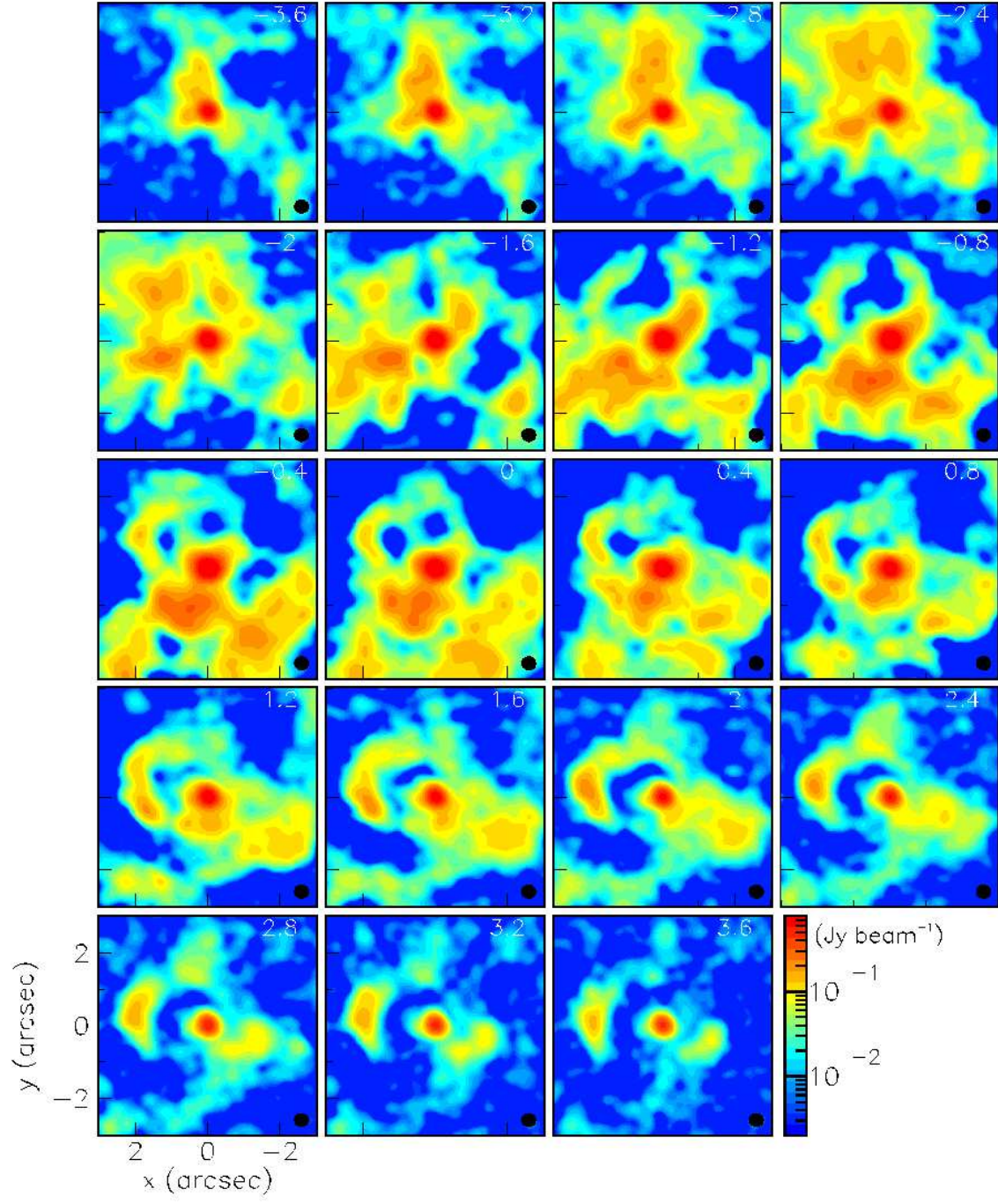


Figure A1. Channel maps of the $^{13}\text{CO}(3-2)$ emission.